

Received July 7, 2017, accepted August 24, 2017, date of publication September 14, 2017, date of current version October 12, 2017.

Digital Object Identifier 10.1109/ACCESS.2017.2752649

Magnetic Resonance Imaging Assisted by Wireless Passive Implantable Fiducial e-Markers

**SAYIM GOKYAR¹, (Student Member, IEEE), AKBAR ALIPOUR¹, (Student Member, IEEE),
EMRE UNAL¹, ERGIN ATALAR¹, (Senior Member, IEEE),
AND HILMI VOLKAN DEMIR^{1,2}, (Senior Member, IEEE)**

¹National Magnetic Resonance Research Center (UMRAM), Department of Electrical and Electronics Engineering, UNAM-Institute of Material Science and Nanotechnology, Bilkent University, Ankara TR-06800, Turkey

²Luminous! Center of Excellence for Semiconductor Lighting and Displays, School of Electrical and Electronic Engineering, School of Physical and Mathematical Sciences, Physics, Nanyang Technological University, Singapore

Corresponding author: Sayim Gokyar (sayim@ee.bilkent.edu.tr)

This work was supported by UNAM, TÜBA and TUBITAK-BIDEB.

ABSTRACT This paper reports a wireless passive resonator architecture that is used as a fiducial electronic marker (e-marker) intended for internal marking purposes in magnetic resonance imaging (MRI). As a proof-of-concept demonstration, a class of double-layer, sub-cm helical resonators were microfabricated and tuned to the operating frequency of 123 MHz for a three T MRI system. Effects of various geometrical parameters on the resonance frequency of the e-marker were studied, and the resulting specific absorption rate (SAR) increase was analyzed using a full-wave microwave solver. The B_1^+ field distribution was calculated, and experimental results were compared. As an exemplary application to locate subdural electrodes, these markers were paired with subdural electrodes. It was shown that such sub-cm self-resonant e-markers with biocompatible constituents can be designed and used for implant marking, with sub-mm positioning accuracy, in MRI. In this application, a free-space quality factor (Q -factor) of approximately 50 was achieved for the proposed resonator architecture. However, this structure caused an SAR increase in certain cases, which limits its usage for *in vivo* imaging practices. The findings indicate that these implantable resonators hold great promise for wireless fiducial e-marking in MRI as an alternative to multimodal imaging.

INDEX TERMS Magnetic resonance imaging, wireless resonators, fiducial e-markers, implants.

I. INTRODUCTION

Magnetic resonance imaging (MRI) has been attracting increasing interest for the localization of implantable devices (e.g. subdural electrodes). Although the soft tissue contrast of MRI [1] makes it the strongest tool among other imaging modalities (including X-ray, CT, and PET), the positioning of devices under MRI requires special treatment, such as employing wired connections [2]–[4] and [5], introducing MRI marker materials [6]–[10] and [11] using wireless passive devices with inductive coupling [12], [13].

Using wired connections to electrically reach implanted devices under MRI is limited to interventional applications [14] and comes at the cost of increased radiofrequency (RF) heating risk [15]. Using ¹H-containing MRI visible marker materials such as bearings [6], [7], vitamin-E capsules [8] and dyes [9], [10], has other disadvantages, including physical attachment to the imaged object, size and non-adjustable relaxation parameters. These markers

typically have sizes of several mm in three dimensions, which limits their *in vivo* usage for most clinical applications, such as subdural electrode marking. Additionally, once they are manufactured, the longitudinal (T1) and transverse (T2) relaxation times of these markers will be constant, and their visibility will strictly depend on the MRI parameters, including repetition time (TR) and echo time (TE). This may limit the imaging methods; hence, additional scans with proper TR and TE values should be performed for marking of fiducial devices. Simultaneous imaging of marking materials and anatomical features is critical to achieve better registration accuracy [16].

In addition to these methods, multimodal imaging is also used to mark the locations of the subdural electrodes [17]–[20]. However, the registration of images that are acquired from different platforms results in reliability problems due to larger positioning errors typically ranging from 1 to approximately 3 mm [21], [22]. In addition to the

reliability problems, switching the patient from one platform to another also decreases the patient’s comfort and increases the risk of inflammation. The ability to image implantable devices using only MRI will avoid the need for multimodal imaging platforms, which will result in improved clinical practice.

The use of wireless resonant devices is potentially highly promising for marking implantable devices without requiring multimodal imaging. MRI performance of these wireless markers is loosely dependent on the imaging parameters (TR, TE and resolution). However, the use of e-markers requires novel resonator designs for proper operation. Physical dimensions of these markers together with RF safety concerns should be considered for the surrounding tissues [15]. Decreasing RF power is a good practice to prevent patients from the harmful effects of RF exposure, but this undesirably leads to a lowered signal-to-noise-ratio (SNR) on the acquired MRIs and decreases the reliability of images for diagnoses, especially for regions with lower proton densities.

In this work, we designed and demonstrated an innovative structure that alleviates the potential complications of the previous works in the literature and can be used as a wireless MRI marking device for potential in vivo studies, such as marking subdural electrodes. Here, we address the scientific challenge of achieving a low footprint area and high Q-factor simultaneously for a 123 MHz self-resonance frequency. As a proof-of-concept demonstration, we achieved an 8 mm × 8 mm footprint area with a free-space Q-factor of approximately 50 for the given operational frequency. Here, we also report the simulation results of the specific absorption rate (SAR) increase in the brain. Ex-vivo MR images support that the proposed architecture is an excellent candidate for wireless electronic markers (e-markers). This may create new possibilities for next-generation implants that contain integrated wireless e-markers.

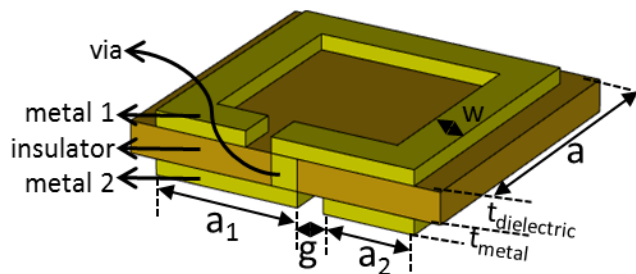


FIGURE 1. Schematic layout of the proposed design (not drawn to scale).

II. THEORY

The proposed e-marker architecture, illustrated in Fig. 1, is a thin film loaded double-layer helical structure that can be fabricated in its multilayer form or in the form of incomplete turns. Instead of stacking independent split-ring resonators (SRR) among different layers [23], this structure combines them with a proper via metallization to increase the effective inductance (L_{eff}), and thus further decreases

the resonance frequency to compensate for MRI applications without compromising the footprint area.

For electrically very small systems, the circuit theory approach becomes reasonable to model the basic characteristic parameters. Hence, the Q-factor of the resonator shown in Fig. 1 can be expressed as:

$$Q = \frac{\omega_0 L_{eff}}{R_{eff}} \tag{1}$$

where ω_0 is the angular frequency, L_{eff} is the effective inductance and R_{eff} is the effective resistance of the resonator.

The most important component of this device is the via-metallization that connects the opposite sides of the resonator between different layers, allowing for strong inductive coupling. As deduced from [24], the approximate effective inductance and resistance of the given design can be formulated as:

$$L_{eff} = n^2 L_0 \tag{2}$$

$$R_{eff} = n R_0 \tag{3}$$

where L_0 is the inductance of a single layer, n is the number of turns, and R_0 is the resistance of a single turn. By substituting (Eqn. 2 and 3) into (Eqn. 1), we obtain:

$$Q = \frac{\omega_0 n^2 L_0}{n R_0} = n \frac{\omega_0 L_0}{R_0} = n Q_0 \tag{4}$$

concluding that the Q-factor is increasing with the number of turns for this special structure at a constant pre-determined operating frequency [25]. Increasing the number of turns for conventional structures (e.g., spirals, solenoids and SRRs) will not linearly increase the quality factor due to lowered inductance for the consecutive turns [26]. Hence, this geometry is very special in terms of the high quality factor and built-in capacitance to be tuned to pre-determined MRI frequency.

The effective parallel plate capacitance (C_{eff}) created between consecutive layers is also used to tune the operational frequency of this geometry to a pre-defined MRI frequency and avoids the need for the use of external capacitors, enabling ultra-thin and flexible structures. With this design, it is possible to create very large capacitance values using conventional fabrication methods to tune this structure to a broad range of frequencies to be used for different applications.

III. MATERIALS AND METHODS

Unlike wired antenna systems used in MRI, this wireless resonator does not require complicated electronics to match any input impedance level. This removes the burden of matching capacitors, resulting in more compact solutions with lowered artifacts. Tuning the resonance frequency of a wireless resonator to a pre-defined MRI frequency becomes challenging when there is no space for the lumped elements (e.g. capacitors and inductors). Regarding the engineering design, as well as geometric parameters, it is important to simultaneously achieve a low footprint area, decreased resonance frequency and higher quality factor.

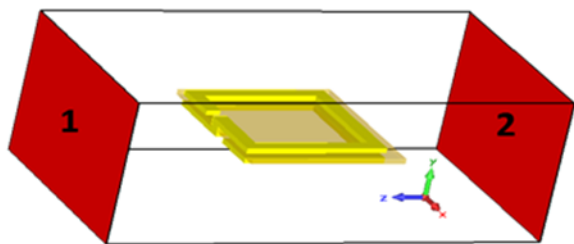


FIGURE 2. Simulation environment to obtain RF characterization of the proposed design.

A. NUMERICAL SIMULATION ENVIRONMENT

To understand the effect of different design parameters on the resonance frequency, we used CST-Design Studio™ (Computer Simulation Technologies, Darmstadt, Germany). Fig. 2 depicts the simulation environment for the proposed structure with two ports located in the z -direction that are consecutively labeled 1 and 2.

Scattering parameters (S_{11} and S_{21}) were obtained, with boundary conditions of the perfect-electrical-conductor (PEC), perfect-magnetic-conductor (PMC) and perfectly matched layer in the x , y and z directions, respectively. The simulation environment was extended with the side length of the resonator (e.g., 8 mm in this case) in all directions. Polyimide material from the library of the numerical solver was used as the dielectric layer with a variable thickness ($t_{dielectric}$), and gold (Au) was used as the metal layer with a variable metallization width (w). Both $t_{dielectric}$ and w were swept over a range of values to understand their effect on the resonance frequency of the resonator.

To verify the superiority of the present architecture, we simulated a 3-D body model from the library of the CST Microwave Studio™, using a birdcage coil with a diameter of 70 cm and a length of 120 cm tuned to 123 MHz. It has previously been shown that the tissue parameters (hence, RF characteristics) of adults and children [27] and [28] and the performance levels of different solvers [29] are not considerably different from each other. Thus, we used a child's body model to decrease the computational burden as a result of the reduced tissue volume. Numerical SAR results were acquired using a time domain solver and a power loss monitor. Time-averaged SAR values were calculated by using the time derivative of the incremental energy (absorbed by an incremental mass of 1 and 10 g of tissues).

B. MRI EXPERIMENT SETUP

MRI measurements were taken using a 3 T Siemens Tim Trio System (Siemens Healthcare GmbH, Erlangen, Germany) with a body-mimicking liquid phantom composed of 2 mM copper sulfide solution ($\text{CuSO}_4 \cdot 5\text{H}_2\text{O}$, with 98% purity of Merck) and 50 mM of NaCl, which mimics most tissues [30], with a relative permittivity of approximately 60, conductivity of 0.5 S/m [31], T_1 of 114 ms and T_2 of 82 ms. The characteristic parameters of this phantom are suitable to analyze the in vivo loading performance of

the resonator. Here, initial images were acquired by using the body coil as the transmitter and the standard twelve-channel head coil as the receiver using a spoiled gradient echo sequence (also known as gradient-recalled echo, GrE), with a $100 \text{ mm} \times 100 \text{ mm}$ field of view (FOV) in the transverse plane, 256×256 image resolution, 2 mm slice thickness, TR/TE of 100 ms/10 ms, 260 Hz pixel bandwidth, a flip angle of 10° and total imaging duration of 29 s. To extract the experimental B_1^+ map for the double-angle method [32], we used two saturated GrE images with flip angles of 10° and 20° .

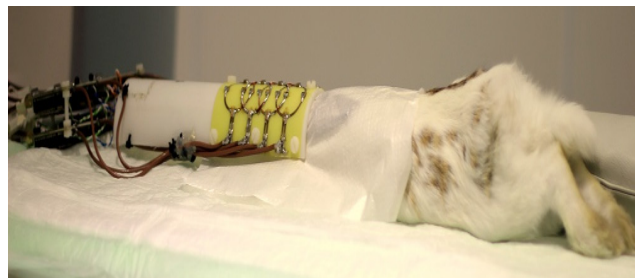


FIGURE 3. An eight-channel open surface coil system used for ex-vivo animal studies.

As a proof-of-concept demonstration, we prepared an imaging environment with an eight-channel open surface coil array, dedicated to animal experiments, and a rabbit used for ex-vivo imaging was placed in the scanner as shown in Fig. 3. Necessary steps were taken to follow the national laws (5199, February, 2014), ruled by the European Union Directive 2010/63/EU, for animal experiments. The rabbit was positioned on the patient bed of the scanner and transverse images were acquired for marking purposes. Images were acquired by using the body coil as the transmitter and the surface coil as the receiver with GrE sequence, $100 \text{ mm} \times 100 \text{ mm}$ FOV in the transverse plane, 256×256 image resolution, 2 mm slice thickness, TR/TE of 100 ms/10 ms, 260 Hz pixel bandwidth, a flip angle of 3° and total imaging duration of 29 s.

Marking precision of the marker-electrode pair was studied by using methods provided in the literature [33]. One of two pairs of electrodes was stabilized to the iso-center of a polycarbonate container and used as the reference point for MRI positioning; the second electrode pair was translated along the imaging plane (coronal) by using the grid points of the phantom-filled container. We used a GrE sequence (TR = 100 ms, TE = 10 ms, flip angle = 10° , slice thickness = 3 mm, FOV = $220 \text{ mm} \times 220 \text{ mm}$) to acquire the position of the translated marker-pair, which was compared to the reference by using 2D Gaussian fit. The actual position was measured by using a ruler and the estimated position was obtained from the MR images for different resolutions. The errors between the actual and estimated positions of the pairs were calculated in two dimensions. Euclidian distance was obtained from these two orthogonal directions to acquire the resulting marking accuracy.

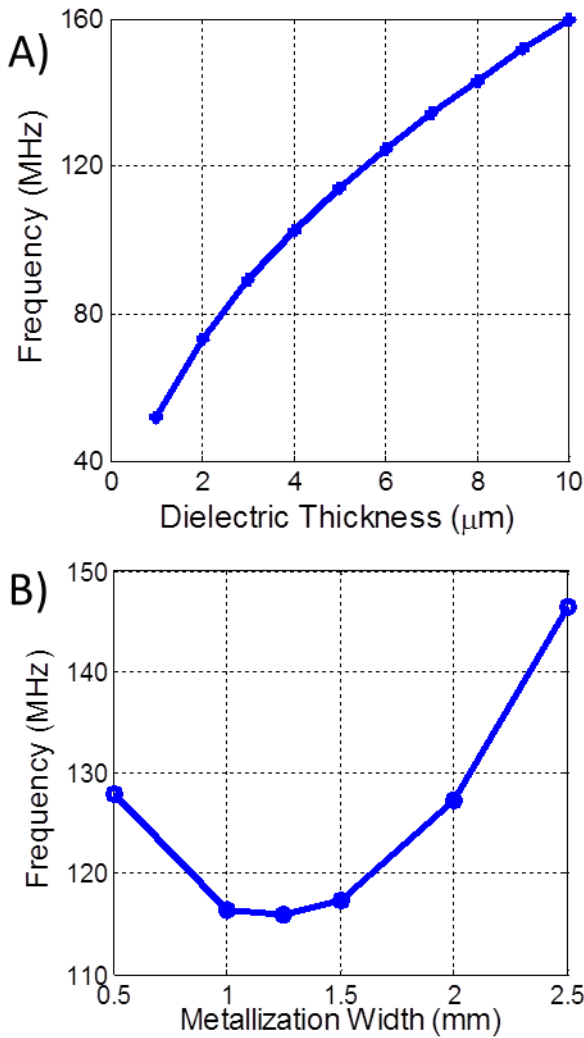


FIGURE 4. Resonance frequency characteristics of the proposed design: (A) due to dielectric thickness and (B) due to metallization width.

IV. RESULTS AND DISCUSSION

A. FREQUENCY TUNING

For the constant footprint area (8 mm × 8 mm for this application), it is possible to change the parameters w , t_{diel} , metallization thickness (t_{metal}), gap width (g) and comb sizes (a_1 or a_2). It is obvious that the thin-film capacitance mainly depends on w and $t_{dielectric}$, while the other parameters affect the quality factor (e.g., t_{metal}) and field confinement volume (e.g. g and a_1). Here, we swept values of $t_{dielectric}$ from 1 to 10 μm and w from 0.5 to 2.5 mm with the abovementioned simulation domain parameters to acquire the resonance frequencies.

Fig. 4A shows the results of the various dielectric thicknesses for a fixed w (0.5 mm). The thin-film capacitance is inversely proportional to the dielectric thickness. Thus, thinner dielectrics confine higher electric field intensities to achieve higher thin-film capacitance, resulting in lowered resonance frequency. With this dielectric thickness range, it is possible to cover the 1.5 T (e.g., 64 MHz) and 3.0 T (e.g., 128 MHz) MRI frequencies.

Fig. 4B shows the resonance frequency as a function of w for a fixed dielectric thickness ($t_{diel} = 7.5 \mu\text{m}$). The effect of w on the resonance frequency is more complicated than that of $t_{dielectric}$. Increasing w increases the parallel plate surface area, resulting in increased thin-film capacitance. However, it also lowers the effective inductance [24] and the quality factor (see Eqn. 5) of the overall structure. Since the resonance frequency is inversely proportional to the multiplication of effective inductance and capacitance, it will reach a minimum due to the maximum of this product. Hence, it is important to be careful when adjusting metallization width to decrease the resonance frequency.

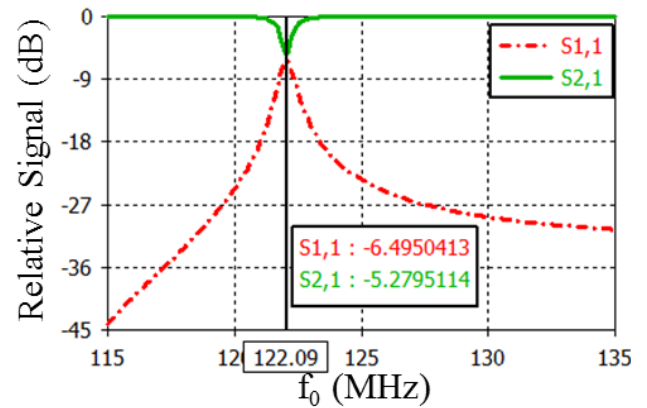


FIGURE 5. Resonance frequency characteristics of the tuned structure for $a = 8 \text{ mm}$, $w = 1 \text{ mm}$, $t_{dielectric} = 7.5 \mu\text{m}$, $t_{metal} = 10 \mu\text{m}$, $g = 1 \text{ mm}$, $a_1 = 4.5 \text{ mm}$ and $a_2 = 2.5 \text{ mm}$.

For our case, the optimal w/a ratio is approximately 0.12 in which the resonance frequency drops to its minimum. For our experimental use, we set the w/a ratio as 0.125 (e.g., $w = 1 \text{ mm}$ for $a = 8 \text{ mm}$) with a higher inductance value to keep the quality factor reasonably high. To finalize our design, we selected $w = 1 \text{ mm}$, $a = 8 \text{ mm}$, $a_1 = 4.5 \text{ mm}$, $a_2 = 2.5 \text{ mm}$, $g = 1 \text{ mm}$, $t_{dielectric} = 7.5 \mu\text{m}$ (due to the thickness of Kapton HN-30) and $t_{metal} = 10 \mu\text{m}$ (due to the skin depth of EM waves at 123 MHz). Fig. 5 shows the numerical results for the scattering parameters of the proposed architecture with the above dimensions and simulation environment. The tuned structure’s resonance frequency was approximately 122 MHz with a strong resonance behavior.

B. MICROFABRICATION AND RF CHARACTERIZATION

We microfabricated a resonator onto an 8 mm × 8 mm footprint area by using a Kapton® (HN 30, Dupont, Wilmington, Delaware, USA) polyimide film with a thickness of 7.5 μm as the dielectric layer sandwiched between the metal lines. Before starting the metallization process, we cleaned the substrate with oxygen plasma. By using a hard-mask with asymmetric comb sizes ($a_1 = 4.5 \text{ mm}$, $g = 1 \text{ mm}$ and $a_2 = 2.5 \text{ mm}$), we thermally evaporated two 10 μm thick Ti/Au metals, on opposite sides of the Kapton® film, and additionally introduced a cross-connection via metallization

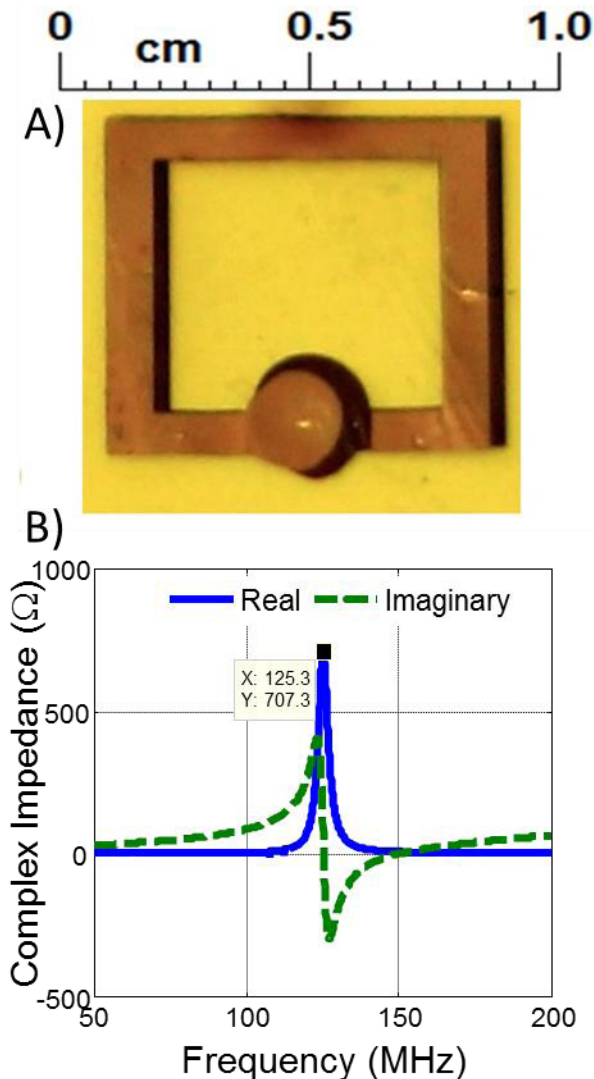


FIGURE 6. Microfabricated device: (A) Optical image of the device fabricated onto flexible polyimide and (B) RF characterization of the same device for resonance frequency determination.

through a gap in the substrate, joining opposing pairs of edges from the metallization layers on the two sides. Then, a $20\ \mu\text{m}$ thick Polydimethylsiloxane (PDMS) layer was coated on both sides for electrical isolation of the conductive layers from the tissues. A microfabricated device is presented in Fig. 6A.

Experimental RF characterization of the microfabricated resonators was carried out by using standard methods provided in the literature [34]. Input impedance of the pick-up coil, which has the same footprint area as the marker, was measured with a network analyzer (Agilent E5061B, Agilent, Santa Clara, California, USA). In the impedance graph presented in Fig. 6B, which was extracted from the input impedance of the pick-up coil, we find the resonance frequency of the fabricated e-marker to be 125.3 MHz with a corresponding free-space wavelength (λ_0) of 2.39 m. By using the full-width-half-maximum (FWHM) of the impedance graphs in Fig. 6B, we calculated a quality

factor of approximately 50 for this resonance frequency. Similarly, a resonator-electrode pair was measured with the same method resulting in a loaded Q-factor of 42 that means a small decrease in the Q-factor, which is in agreement with previous results [35]. We found that the side length of the resonator (8 mm) was approximately $\lambda_0/300$, which is one of the smallest single-chip deep-subwavelength resonators described in the literature that does not use a lumped element [26].

Resonance frequency estimation by using numerical methods deviated only 3 MHz from the measurement results, which might be due to dielectric coefficient differences of the material available in the library. Another possible reason for this deviation is the misalignment of consecutive layers, which decreases effective capacitance. Hence, this results in an increased resonance frequency for the experimental case. These results are in good agreement with each other, indicating that the MRI frequencies for most of the clinical systems (1.5 and 3 T) are easily achievable.

Reaching lower resonance frequencies is feasible for this architecture, and tuning to higher frequencies can be accomplished by simply partially etching one of the metallization layers. We would deduce that resonance frequencies from 70 MHz to 5.5 GHz are possible by simply using the same structure, as the self-resonance frequency increases to 5.5 GHz for a single-layer loop resonator with these dimensions. The superiority of the given architecture, specifically achieving ultra-wide-band tuning performance, allows it to be used as a fiducial marker for a wide range of MRI frequencies.

C. NUMERICAL RESULTS FOR FIELD DISTRIBUTIONS

Fig. 7A presents the normalized surface current distribution (\vec{J}_c distribution normalized to the incident magnetic field), whereas Fig. 7B shows the normalized electric field map ($|\vec{E}|$ field normalized to incident electric field) at the dielectric layer between conductive metallization layers for the resonance frequency of 123 MHz. From Fig. 7A, we can infer that the magnetic field, coupled to the resonator at its resonance frequency, causes a surface current improvement (by 25-fold for this architecture) on the metallization layers. This results in improved B_1^+ field distribution, which explains the SNR improvement in the MR images.

Using a resonator in a lossy medium (e.g., inside a biological tissue) introduces challenges due to the loading of the resonator. Lossy medium leads to a decreased quality factor and an increased SAR for the surrounding tissue. At this point, the E-field distribution, as illustrated in Fig. 7B, indicates that the electric field is confined to the dielectric layer between the metallization layers and does not spill over to the surrounding tissue. This allows for a reduction of the interaction between the proposed structure and the environment. Therefore, we would foresee that the performance of the resonator is improved in terms of loading and SAR parameters compared to conventional resonator architectures.

As depicted in Fig. 8A, we computationally calculated the normalized B_1^+ map on the transverse plane by passing

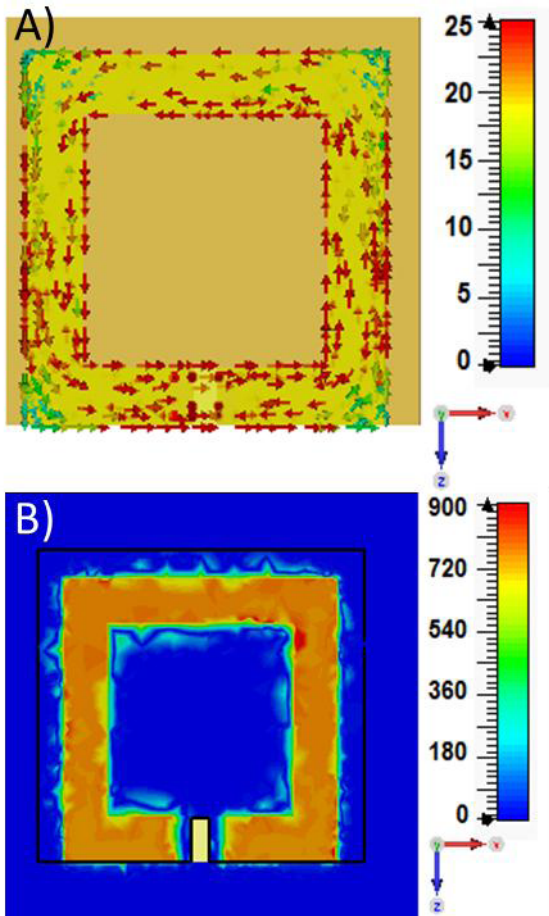


FIGURE 7. Normalized field distributions for the resonator plane: (A) Normalized surface current distribution of the resonator and (B) normalized electric field distribution in the middle layer of the dielectric. It is clearly shown that the electric field is strongly confined between the metallic layers.

through the resonator from its center, which is normalized to the simulated power. From the simulation results, we verified that the amplitudes of the B_1^+ and B_1^- maps are similar, which is expected due to the nature of the reciprocal wireless passive resonator architectures. We achieved $500 \mu T$ of the B_1^+ field amplitude for a 1 kW simulated input power.

Fig. 8B depicts the $|H|/|E|$ ratio of the given e-marker for the same plane as indicated in Fig. 8A. Fig. 8B quantitatively visualizes the ratio of magnetic to electric field distributions, which should be approximately $1/\eta$ for the given numerical configuration (i.e. approximately $\sqrt{60/377} = 0.02$ (A/V) for the plane wave propagation). When we move away from the resonator, we would see that the H/E ratio drops to its normal value (0.02 A/V), whereas it is almost 5 times higher (0.10/0.02) in the resonator vicinity. Since the magnetic field is proportional to image intensity and the electric field is proportional to SAR, the SNR improvement will always be more than the SAR increase for this tissue loading configuration.

Unlike conventional resonators, our proposed architecture successfully confines the E-field between its metallic layers, while increasing the B_1^+ field in its vicinity to successfully

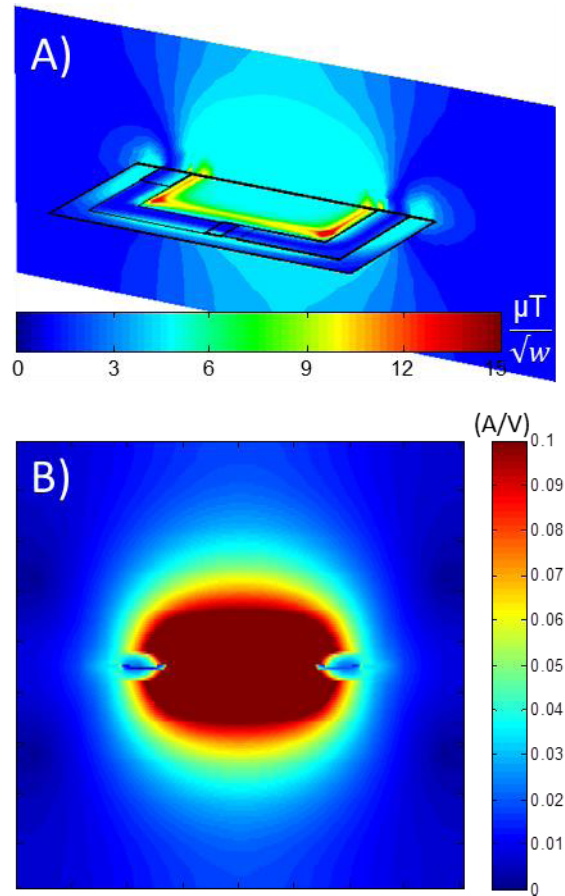


FIGURE 8. Field maps of the proposed design for the transverse plane. (A) Numerical B_1^+ map and (B) $|H|/|E|$ ratio (A/V) map.

achieve its marking purpose. From these results, we see that the MRI performance of the proposed structure is comparable to those of traditional wireless coils as reported in the literature [35].

D. SAR CHARACTERIZATION WITH PHANTOM SIMULATIONS

By using the child phantom from the library of the CST, we computed the SAR distribution in the head of the given data set. Fig. 9A and 9C show the SAR maps of the imaged subject for the sagittal plane that includes the region of the highest SAR with 1 and 10 g averaging, respectively. To understand the effect of resonator, we located it at the point with the highest SAR and ran the solvers to compute secondary SAR maps, as illustrated in Fig. 9B and 9D. These results show that the SAR is increased from 1.09 to 1.91 W/kg for 1 g of averaging and 0.763 to 1.22 W/kg for 10 g of averaging. These numbers should be considered to determine the upper limit of the applied RF power for the imaging sequences for the patients with such a resonator. Within this limit, the resonator will outperform the resonator-free case by more than an order of magnitude in terms of the image intensity, indicating the substantial benefit in its usage.

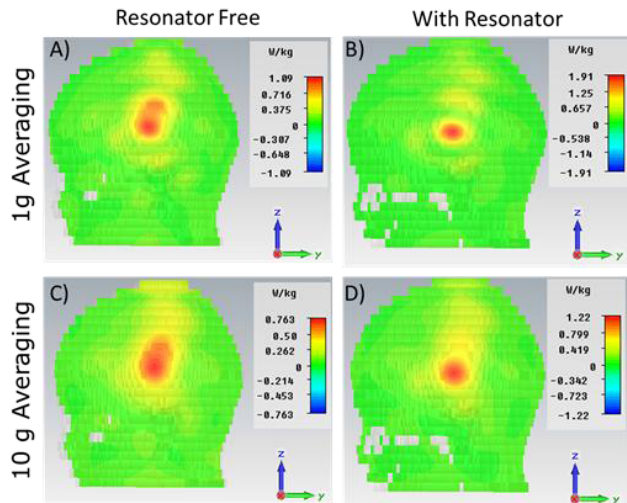


FIGURE 9. SAR distribution results of the given design for the child data set: (A) 1 g of averaging without resonator, (B) 1 g of averaging with resonator, (C) 10 g of averaging without resonator and (D) 10 g of averaging with resonator.

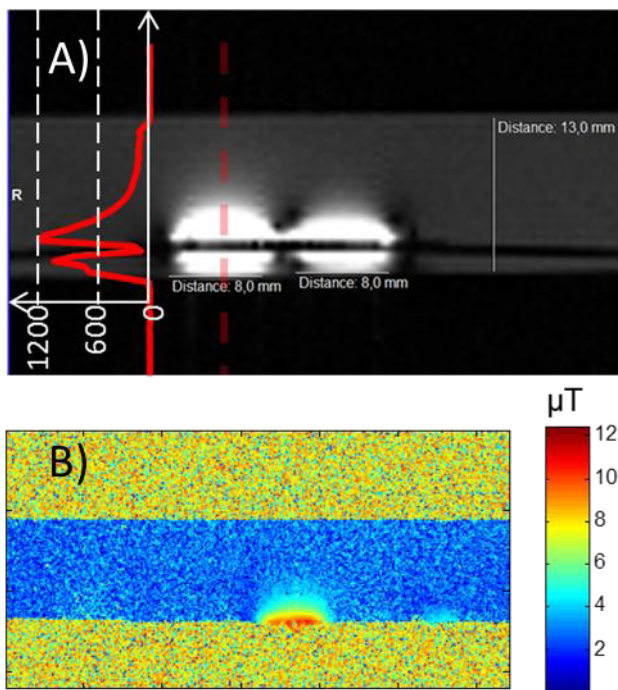


FIGURE 10. Experimental characterization of the proposed e-marker: (A) MRI of the proposed designs that are placed 2 mm away from each other and consecutively fabricated onto the same dielectric. (B) B_1^+ map of the given e-marker, which was computed using the double-angle method.

E. EXPERIMENTAL MRI CHARACTERIZATION

Fig. 10A shows the MRI of the fabricated devices, immersed in the phantom described above, using the GrE sequence and a flip angle of 10° . The provided MRI depicts that the signal intensity is higher in the vicinity of the resonators, which is also proportional to the B_1^+ field distribution provided in Fig. 8A. The signal intensity profile along with the dashed

TABLE 1. Positioning accuracy of the proposed marker.

| Image Matrix | Pixel Size (mm) | μ_x (mm) | μ_z (mm) | μ_r (mm) |
|------------------|-----------------|--------------|--------------|--------------|
| 64×64 | 3.44 | 2.09 | 2.18 | 2.06 |
| 128×128 | 1.72 | 1.84 | 1.96 | 1.83 |
| 256×256 | 0.86 | 1.25 | 1.38 | 1.26 |
| 384×384 | 0.57 | 0.94 | 1.05 | 1.02 |
| 512×512 | 0.43 | 0.64 | 0.72 | 0.71 |

red line passing through the center of a resonator is presented on the left side. It is clearly shown that the signal level is amplified by an order of magnitude in the vicinity of the resonator, which results in an approximately 15-fold SNR improvement.

The brightness of certain regions close to the resonator can be seen, which occurs because of two reasons: 1) the inductive coupling of the transmit-field (B_1^+ improvement) and 2) the receive-field inductive coupling. The applied RF power induces surface currents proportional to the resonator Q-factor, which in return creates an effective B_1^+ field distribution in its vicinity ($B_{IQ}^+ \sim Q \cdot B_1^+$). The new flip angle (α) distribution will be proportional to this new B_{IQ}^+ field distribution ($\alpha \sim \gamma B_{IQ}^+ \tau$, where γ is the gyromagnetic ratio). Hence, the transmit field contribution to the imaging signal will be proportional to $\sin(\alpha) \sim \sin(\gamma Q B_1^+ \tau)$ [36]. Thus, the image intensity distribution will depend on the quality factor and the B_1^+ distribution due to the spatial distribution of this flip angle.

Fig. 10B shows the experimental B_1^+ map distribution that was computed using the double-angle method [32]. Here, we see that the B_1^+ field is almost 6 times higher ($12 \mu\text{T} / 2 \mu\text{T}$) in the vicinity of the resonator compared to remote points.

Once the spins are excited in the presence of a resonator, they emit a precise signal that is captured by the resonator and transmitted to the receiver antennas. This process, known as receive-field coupling, is proportional to the Q-factor of the resonator [37]. Hence, the overall image intensity enhancement profile will be proportional to the multiplication of these two effects. ($I_Q = |I_0 Q \sin(\alpha)|$, here note that α is position dependent).

Marking precision results are reported in Table 1. Here, μ_x and μ_z are the mean of absolute errors between the actual and measured positions in x and z directions respectively, whereas μ_r is the mean error of the Euclidian distance. Increasing the resolution of the acquired images allows us to position the marker more precisely. We can infer that the sub-mm positioning accuracy using a reference marker-resonator pair can be achieved, which is comparable to previously reported results [16].

F. SUBDURAL ELECTRODE MARKING

Subdural electrodes are commonly used in epilepsy diagnoses to successfully determine the sites for recession in the

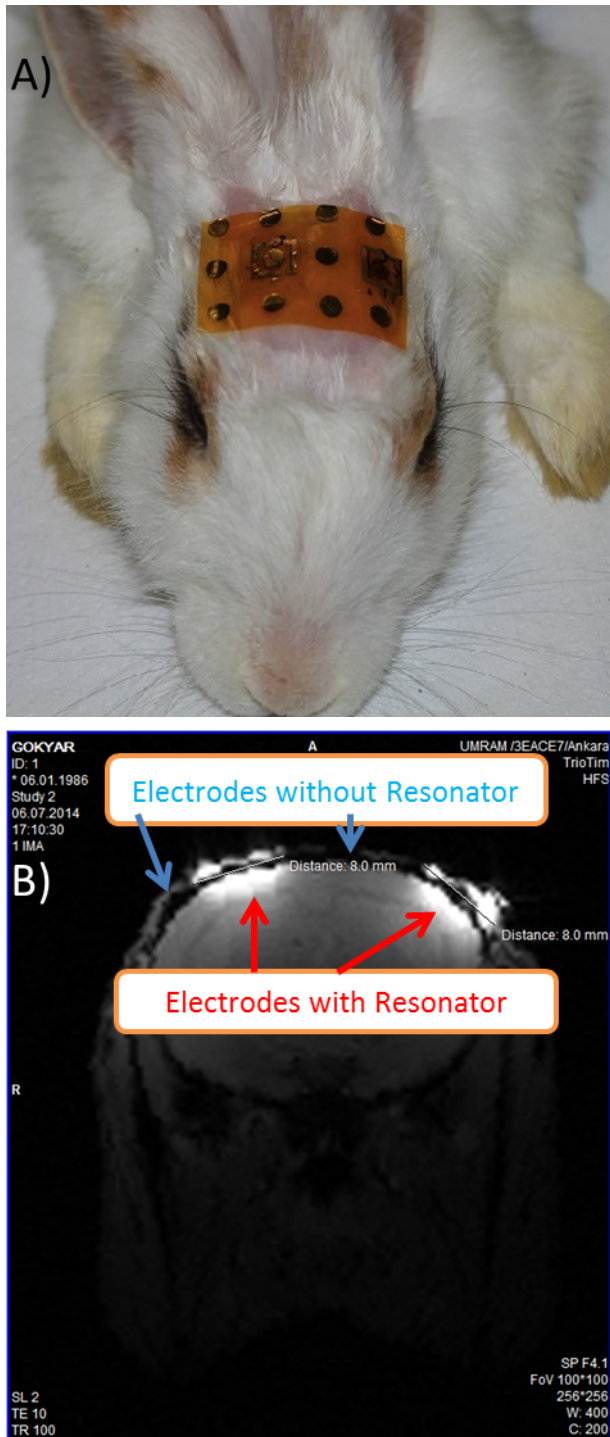


FIGURE 11. MRI of the proposed resonator-electrode pairs for ex-vivo applications: (A) Optical image of the rabbit with a resonator-electrode pair positioned on its head. (B) MRI of the brain for the given imaging configuration. Vicinity of electrode-resonator pair is clearly visible and marked on the same image.

brain [38]. As mentioned earlier, clinical MRI scans are not suitable to show these electrodes due to the lack of ^1H atoms in their content. Some magnetic content could be added to these electrodes to make them MRI visible (actually darker), but this comes with a loss of data and increased artifacts

near them. Positions of the non-magnetic subdural electrodes cannot be determined by MRI, so additional imaging modalities, e.g., X-ray, PET and CT, are required to correctly determine their locations. The proposed e-marker removes this multi-modal imaging effort by its high-quality resonance characteristics.

Although a detailed analysis of the safety of intracranial EEG electrodes under MRI was previously conducted [39], their magnetic content prevents the use for GrE sequences. Hence, we fabricated an array of mimicked non-magnetic subdural electrodes. To mimic the operation of subdural electrodes, we deposited Ti/Au metals onto a $12.5\ \mu\text{m}$ thick flexible polyimide film with a diameter of 4 mm and combined them with the resonators by sticking them to each other. The overall electrode-resonator pair was placed externally on the head of a rabbit as shown in Fig. 11A.

Standard gradient echo sequences with different imaging parameters were applied to verify the operation of the resonator. Although we presented the MRI that is acquired by using a flip angle of 3° in Fig. 11B, we observed that it would be as low as 1° or as high as 60° for this configuration. MRIs showed that we were able to clearly mark these electrodes with resonators whereas the other electrodes without resonators could not be distinguished in the image as shown in Fig. 11A. The resulting performance of the resonators is high even in the vicinity of the electrodes. Not only is marking possible but also SNR enhancement, which can be clearly seen in Fig. 11B. By adding resonators onto all of the electrodes, it would be possible to map each electrode using only MRI. All of the complications regarding the transportation of patients, mapping of electrodes, and use of CT, PET or X-ray imaging to obtain clear positioning of electrodes can thus be resolved, and positioning efforts can be significantly simplified.

V. CONCLUSION

We proposed, designed, fabricated and successfully demonstrated an MRI-visible high-quality resonator system that is flexible, smaller and potentially biocompatible to be used for in vivo applications including subdural electrode imaging. Variants of the proposed resonator can be used in interventional MRI devices and future MRI-visible smart implants. This architecture enables miniaturization down to sub-cm sizes ($8\ \text{mm} \times 8\ \text{mm}$ in this work) without sacrificing its practical usage and performance. The proposed structure benefits from the high inductance of a helical ring and the high parallel plate capacitance of multiple layers for the same conductive path. Its frequency response can be conveniently tuned within sub-cm footprint limits such that the operating frequency of the resonators can be in resonance with the imaging frequencies of clinical MRI devices simply by changing the metallization width, dielectric film thickness, and number of layers or any combination of these parameters.

Although the present design causes SAR to increase by approximately 90%, without exceeding the FDA or IEC standards for most of the clinical applications, it increases

SNR by over 15 times for the reported imaging practices and by approximately 5-fold for most of the clinical applications. All of these results indicate that the proposed architecture holds great promise to be used in MRI to improve the image intensity and, hence, the SNR in its vicinity. The proposed architecture does not limit conventional clinical practices, such as using PET and CT for the imaging of metallic objects, or the imaging parameters such as TR and TE.

Integration of the proposed resonators with implants (e.g. subdural electrodes) during fabrication would further improve the operational reliability of the devices and allow for in vivo studies, which will be considered as a future step. Additionally, in future work, although the essential constituents of the proposed structure (Ti, Au, and PDMS) are all individually biocompatible, the biocompatibility of the overall structure should be verified before in vivo experiments.

ACKNOWLEDGMENTS

The authors of this work would like to thank Mr. Taner Demir for his help in preparing the open coil system, Dr. Volkan Acikel for his valuable discussions about phantom recipes, and Prof. Kader Karli Oguz M.D. and Prof. Burçak Bilginer M.D. for their recommendations and discussions regarding intracranial electrodes.

REFERENCES

- [1] P. C. Lauterbur, "Image formation by induced local interactions: Examples employing nuclear magnetic resonance," *Nature*, vol. 242, pp. 190–191, Mar. 1973.
- [2] E. Atalar et al., "High resolution intravascular MRI and MRS by using a catheter receiver coil," *Magn. Reson. Med.*, vol. 36, pp. 596–605, Oct. 1996, doi: 10.1002/mrm.1910360415.
- [3] R. R. A. Syms, I. R. Young, C. A. Wadsworth, S. D. Taylor-Robinson, and M. Rea, "Magnetic resonance imaging duodenoscope," *IEEE Trans. Biomed. Eng.*, vol. 60, no. 12, pp. 3458–3467, Dec. 2013.
- [4] R. R. A. Syms, I. R. Young, M. M. Ahmad, M. Rea, C. A. Wadsworth, and S. D. Taylor-Robinson, "Thin-film detector system for internal magnetic resonance imaging," *Sens. Actuators A, Phys.*, vol. 163, pp. 15–24, Sep. 2010.
- [5] K. Segkhoodhod, R. R. A. Syms, and I. R. Young, "Design of magneto-inductive magnetic resonance imaging catheters," *IEEE Sensors J.*, vol. 14, no. 5, pp. 1505–1513, May 2014.
- [6] G. Chen et al., "MRI-visible polymeric vector bearing CD3 single chain antibody for gene delivery to T cells for immunosuppression," *Biomaterials*, vol. 30, pp. 1962–1970, Apr. 2009.
- [7] P. Pang et al., "An MRI-visible non-viral vector bearing GD2 single chain antibody for targeted gene delivery to human bone marrow mesenchymal stem cells," *PLoS ONE*, vol. 8, no. 10, p. e76612, 2013, doi: 10.1371/journal.pone.0076612.
- [8] J. W. Gilbert et al., "Guidance of magnetic resonance imaging and placement of skin-marker localization devices," *J. Neurosurg. Sci.*, vol. 55, no. 2, pp. 85–88, 2011.
- [9] E. R. Cosman and T. S. Roberts, "CT and MRI visible index markers for stereotactic localization," U.S. Patent 6419 680 B1, Jul. 16, 2002.
- [10] J. E. Baumgartner, "MRI-compatible fiducial markers and methods for using the same," U.S. Patent 2015 0011 868 A1, Jan. 8, 2015.
- [11] C. C. Parker, A. Damyranovich, T. Haycocks, M. Haider, A. Bayley, and C. N. Catton, "Magnetic resonance imaging in the radiation treatment planning of localized prostate cancer using intra-prostatic fiducial markers for computed tomography co-registration," *Radioterapy Oncol.*, vol. 66, no. 2, pp. 217–224, 2003.
- [12] M. Burl, G. A. Coutts, and I. R. Young, "Tuned fiducial markers to identify body locations with minimal perturbation of tissue magnetization," *Magn. Resonance Med.*, vol. 36, no. 3, pp. 491–493, 1996.
- [13] H. H. Quick et al., "Wireless active catheter visualization: Passive decoupling methods and their impact on catheter visibility," in *Proc. 13th Int. Soc. Magn. Reson. Med.*, 2005, p. 2164.
- [14] R. R. A. Syms, I. R. Young, M. M. Ahmad, S. D. Taylor-Robinson, and M. Rea, "Magneto-inductive catheter receiver for magnetic resonance imaging," *IEEE Trans. Biomed. Eng.*, vol. 60, no. 9, pp. 2421–2431, Sep. 2013.
- [15] P. A. Bottomley, "Turning up the heat on MRI," *J. Amer. College Radiol.*, vol. 5, no. 7, pp. 853–855, Jul. 2008.
- [16] M. Rea et al., "Sub-pixel localisation of passive micro-coil fiducial markers in interventional MRI," *Magn. Reson. Mater. Phys.*, vol. 22, no. 2, p. 71, 2009, doi:10.1007/s10334-008-0143-1.
- [17] P. S. LaViolette, S. D. Rand, M. Raghavan, B. M. Ellingson, K. M. Schmainda, and W. Mueller, "Three-dimensional visualization of subdural electrodes for presurgical planning," *Neurosurgery*, vol. 68, pp. 152–161, Mar. 2011.
- [18] M. A. Silberbusch, M. I. Rothman, G. K. Bergey, G. H. Zoarski, and M. T. Zagardo, "Subdural grid implantation for intracranial EEG recording: CT and MR appearance," *Amer. J. Neuroradiol.*, vol. 19, pp. 1089–1093, Jun. 1998.
- [19] J. X. Tao, S. Hawes-Ebersole, M. Baldwin, S. Shah, R. K. Erickson, J. S. Ebersole, "The accuracy and reliability of 3D CT/MRI co-registration in planning epilepsy surgery," *Clin. Neurophysiol.*, vol. 120, no. 4, pp. 748–753, 2009.
- [20] S. S. Dalal, E. Edwards, H. E. Kirsch, N. M. Barbaro, R. T. Knight, and S. S. Nagarajan, "Localization of neurosurgically implanted electrodes via photograph–MRI–radiograph coregistration," *J. Neurosci. Methods*, vol. 174, no. 1, pp. 106–115, 2008.
- [21] B. J. Erickson and C. R. Jack, "Correlation of single photon emission CT with MR image data using fiducial markers," *Amer. J. Neuroradiol.*, no. 14, pp. 713–720, May/Jun. 1993.
- [22] M. Nelles, R. Koenig, J. Kandyba, C. Schaller, H. Urbach, "Fusion of MRI and CT with subdural grid electrodes," *Zentralbl Neurochirurgie*, vol. 65, no. 4, pp. 174–179, Nov. 2004.
- [23] M. S. Khennouche, F. Gadot, A. Lustrac, M. P. Quinot, L. Darrasse, and J. C. Ginefri, "The use of metamaterials: A solution to improve the performance of radiofrequency coil for magnetic resonance imaging (MRI)?" *Metamorphose-VI*, vol. 4, pp. 468–470, Oct. 2011.
- [24] F. W. Grover, *Inductance Calculations: Working Formulas and Tables*. New York, NY, USA: Dover, 2004.
- [25] I. Bahl, *Lumped Elements for RF and Microwave Circuits*. Norwood, MA, USA: Artech House, 2003, p. 81.
- [26] F. Bilotti, A. Toscano, and L. Vegni, "Design of spiral and multiple splitting resonators for the realization of miniaturized metamaterial samples," *IEEE Trans. Antennas Propag.*, vol. 55, no. 8, pp. 2258–2267, Aug. 2007, doi: 10.1109/TAP.2007.901950.
- [27] J. Wang and O. Fujiwara, "Comparison and evaluation of electromagnetic absorption characteristics in realistic human head models of adult and children for 900-MHz mobile telephones," *IEEE Trans. Microw. Theory Techn.*, vol. 51, no. 3, pp. 966–971, Mar. 2003.
- [28] E. Conil, A. Hadjem, F. Lacroux, M. F. Wong, and J. Wiart, "Variability analysis of SAR from 20 MHz to 2.4 GHz for different adult and child models using finite-difference time-domain," *Phys. Med. Biol.*, vol. 53, pp. 1511–1525, 2008.
- [29] M. Kozlov and R. Turner, "A comparison of Ansoft HFSS and CST microwave studio simulation software for multi-channel coil design and SAR estimation at 7T MRI," *PIERS*, vol. 6, no. 4, pp. 395–399, 2010.
- [30] *An Internet Resource for the Calculation of the Dielectric Properties of Body Tissues in the Frequency Range 10 Hz–100 GHz*. Accessed: Apr. 16, 2017. [Online]. Available: <http://niremf.ifac.cnr.it/tissprop/>
- [31] V. Acikel, O. Ulutan, A. C. Ozen, B. Akin, Y. Eryaman, and E. Atalar, "A novel MRI based electrical properties measurement technique," in *Proc. Int. Soc. Mag. Reson. Med.*, no. 21, p. 4430, Apr. 2013.
- [32] C. H. Cuningham, J. M. Pauly, and K. S. Nayak, "Saturated double-angle method for rapid B_1+ mapping," *Magn. Reson. Med.*, vol. 55, no. 6, pp. 1326–1333, 2006.
- [33] G. Thörmer, N. Garnov, M. Moche, J. Haase, T. Kahn, and H. Busse, "Simultaneous 3D localization of multiple MR-visible markers in fully reconstructed MR images: Proof-of-concept for subsecond position tracking," *Magn. Reson. Imag.*, vol. 30, no. 3, pp. 371–381, 2012.
- [34] J. C. Ginefri, E. Durand, L. Darrasse, "Quick measurement of nuclear magnetic resonance coil sensitivity with a single-loop probe," *Rev. Sci. Instrum.*, vol. 70, no. 12, p. 4730, 1999.

- [35] J. T. Vaughan and J. R. Griffiths, *RF Coils for MRI*. West Sussex, U.K., Wiley, 2010, pp. 17–25.
- [36] D. G. Nishimura, *The Principles of Magnetic Resonance Imaging*. Stanford, CA, USA: Stanford Univ., Apr. 1996, p. 114.
- [37] S. Wang, J. Murphy-Boesch, H. Merkle, A. P. Koretsky, and J. H. Duyn, “ B_1 homogenization in MRI by multilayer coupled coils,” *IEEE Trans. Med. Imag.*, vol. 28, no. 4, pp. 551–554, Apr. 2009.
- [38] E. Asano, C. Juhasz, A. Shah, S. Sood, and H. T. Chugani, “Role of subdural electrocorticography in prediction of long-term seizure outcome in epilepsy surgery,” *Brain, J. Neurol.*, vol. 132, no. 4, pp. 1038–1047, 2009.
- [39] D. W. Carmichael et al., “Safety of localizing epilepsy monitoring intracranial electroencephalograph electrodes using MRI: Radiofrequency-induced heating,” *J. Magn. Reson. Imag.*, vol. 28, no. 5, pp. 1233–1244, 2008.



SAYIM GOKYAR received the B.Sc. and M.Sc. degrees in electrical and electronics engineering in 2009 and 2011, respectively. He is currently pursuing the Ph.D. degree with the Electrical and Electronics Engineering Department, Bilkent University, Ankara, Turkey. His research interests include wireless sensors and designing implantable devices.



AKBAR ALIPOUR received the Ph.D. degree from the Department of Electrical and Electronics Engineering, Bilkent University, Ankara. His research interests include thin-film microwave structures, which are used for magnetic resonance imaging (MRI) marking and wireless sensing. He has been involved in the development of devices, which are mainly used in interventional MRI and medical implants.



EMRE UNAL received the B.S. degree in electrical and electronics engineering from Hacettepe University, Ankara, Turkey, in 2005. He is currently a Full-Time Research Engineer under the supervision of Prof. H. V. Demir, with the Institute of Materials Science and Nanotechnology, Bilkent University, Ankara, where he is involved in the development of microwave and optoelectronic devices.



ERGIN ATALAR received the B.S. degree from Bogazici University in 1985, the M.S. degree from Middle East Technical University in 1987, and the Ph.D. degree from Bilkent University in 1991, all in electrical engineering. He joined the Johns Hopkins University, where he became a Professor of radiology, biomedical engineering, and electrical and computer engineering and the Director of the Center for Image Guided Interventions. He is currently a Professor with the Department of Electrical and Electronics Engineering and the Director of the National Magnetic Resonance Research Center, Bilkent University. His research interests include magnetic resonance imaging and image guided interventions. In 2006, Ergin Atalar received the TUBITAK Science Award.



HILMI VOLKAN DEMIR (M'04–SM'11) received the B.Sc. degree in electrical and electronics engineering from Bilkent University, Ankara, Turkey, in 1998 and the M.Sc. and Ph.D. degrees in electrical engineering from Stanford University, Stanford, CA, USA, in 2000 and 2004, respectively. In 2004, he joined Bilkent University, where he is currently a Professor with joint appointments with the Department of Electrical and Electronics Engineering and the Department of Physics. He is also with UNAM—the Institute of Materials Science and Nanotechnology. He is a fellow of National Research Foundation in Singapore and a Professor with Nanyang Technological University. His research interests include the development of innovative optoelectronic and RF devices. He was a recipient of the European Union Marie Curie Fellowship, the Turkish National Academy of Sciences Distinguished Young Scientist Award, the European Science Foundation–European Young Investigator Award, and the Nanyang Award for Research Excellence.

• • •